Dyes and Pigments 195 (2021) 109707

Contents lists available at ScienceDirect

Dyes and Pigments

journal homepage: www.elsevier.com/locate/dyepig

Zn(II)-DPA Coordinative fluorescent probe for enhancing G4 DNA binding

Quan-Qi Yu [a], Xue-Xian Lang [a], Juan-Juan Gao [a], Hong-Yao Li [a], Yi-Tong Bai [a], Hai-Jiao Wang [b,**], Ming-Qi Wang [a,*]

[a] School of Pharmacy, Jiangsu University, Zhenjiang, 212013, PR China
[b] The Key Laboratory of Biomedical Material, School of Life Science and Technology, Xinxiang Medical University, Xinxiang, 453003, China

ARTICLE INFO

Keywords:
Zn(II)-DPA
G4 DNA
Carbazole derivate
Fluorescent probe
Cell imaging

ABSTRACT

Novel dipicolylamino functionalized styryl-carbazole derivative (**YCJ**) was designed and synthesized. This derivative in combination with Zn(II) has exhibited large fluorescence intensity enhancement and prominent red-shift in absorption spectra with G4 DNA. Systematical analysis indicats that **YCJ-Zn(II)** complex shows much higher binding affinity and spectral response to G4 DNA than our previously reported styryl-carbazole scaffold (**E1**) due to the incorporationc of a Zn(II)-DPA moiety which could decrease the carbazole core electron density and consequently enhance the ability to display π-π stacking interaction with G4 DNA. Spectroscopic and molecular docking studies have unraveled **YCJ-Zn(II)** complex can stack both 3′ and 5′-ends and an associated with partial loop/groove interactions. The application of this Zn(II) complex as a fluorescent agent for living cell imaging was also demonstrated. The conjugation of the Zn-DPA moiety results in good cell permeability, endogenous DNA labeling, which is suitable for monitoring of nucleus activities.

1. Introduction

Guanine rich DNA sequences fold into tetra-stranded helical assemblies called DNA G-quadruplexes (G4s) [1]. The core structures in the G4s are formed by stacked planar G-tetrads, which are held together via Hoogsteen hydrogen bonds [2]. A series of bio-informatical studies initially suggested that over 700 000 putative G4-forming sequences are abundantly present across the human genome, especially located in the chromosomes and transcriptomes [3–5]. While it is commonly accepted that G4s are involved in a number of essential biological regulatory processes, the exact roles that G4s play in biology are still under significant scrutiny, even providing explicit evidence that G4 structures actually form in native cellular DNA is a formidable challenge [6,7]. Recently, with widespread application in immunofluorescent staining, several G4 structure-specific antibodies such as HF1, BG4, hf2, and 1H6 have been developed to visualize G4s in cells [8–11]. Among these, immunostaining with BG4 in human cells showed the presence of G4 structures in all cell cycle phases, with maximum foci in S phase, which corroborates the replication-dependent formation of G4 [9]. Meanwhile, by developing a quantitative, comparative G4-ChIP-seq methodology, researchers discovered that G4 DNA regions are highly associated with critical drivers of triple-negative breast cancer models [12]. Collectively, G4s could be regarded as a vital biomarker for cancer diagnosis and treatment.

Considering the wide range of biological processes associated with DNA G4s, the requirements for selectively detecting G4 structures are strong motivators for the development tools. Fluorescence imaging has been attracting much more attention in recent years, due to the advantages of fluorescence including simply, high sensitivity, non-destructivity, *in situ* examination, and intracellular detection [13]. Various G4 DNA fluorescent probes have been developed rely on a large enhancement in emission intensity upon binding G4, compared to binding other DNA forms (e.g., duplex, single-stranded DNA). So far, some related review papers have discussed [14–18]. Most probes designed to interact with G4s were initially based on organic compounds, but to a far lesser extent, on metal complexes. It has been shown that metal complexes are attractive G4 DNA binders due to their versatile structural and electronic properties [19–22]. Metal complexes provide the opportunity to access a much wider chemical space than their purely organic counterparts due to the several geometries (e.g., linear, bent, trigonal planar, square planar, tetrahedral, trigonal bipyramidal, octahedral) that coordinated metal ions have [23]. In addition, metal ions can confer unique electronic properties to the system to render the resulting metal complexes with interesting optical, catalytic

* Corresponding author.
** Corresponding author.
E-mail addresses: taiyiyibo@126.com, taiyiyibo@126.com (H.-J. Wang), wmq3415@163.com, wmq3415@163.com (M.-Q. Wang).

https://doi.org/10.1016/j.dyepig.2021.109707
Received 25 May 2021; Received in revised form 3 July 2021; Accepted 5 August 2021
Available online 8 August 2021

or redox properties which in turn can be exploited for imaging or therapeutic applications [24,25]. Several metal complexes are routinely used in the clinic as either therapeutic or imaging agents, with the most prominent example being that of cisplatin and its derivatives for the treatment of various cancers [26,27].

Dipicolylamine (2,2′-dipyridylmethylamine, DPA) is one of the most studied tridentate metal-binding units in coordination chemistry [28–32]. Recently, Zn-DPA complexes attracted considerable attention in biological analysis and cell imaging, through electrically binding the anionic molecular targets [33–35]. Previously, we have developed a fluorescent probe (termed as **E1**) with excellent selectivity to G4s, which possesses a pyridinium side group substituted carbazole planar core through an ethylene bridge (Fig. 1) [36]. However, **E1** has shown to be a switch-on probe for G4s, with moderate fluorescence enhancements and weak cellular potency. Thus, we speculated that by combining the effects of the positively charged Zn-DPA moiety, which can be involved in electrostatic interactions with electronegative regions, and aromatic rings designed to interact through π-stacking, stronger G4 binder may be obtained. Taking into account these highlights, herein, we proposed to link a DPA subunit together with carbazole-pyridinium scaffold to design a new class of G4 DNA ligand **YCJ**. Compared with precursor **E1**, this ligand in combination with Zn(II) has exhibited the improved binding affinity to G4 DNA and enhanced cellular uptake. The effect of Zn-coordination was discussed in detail.

2. Experimental methods

2.1. Materials and instrumentation

A Bruker AM400 NMR spectrometer was used to test the ^{1}H NMR and ^{13}C NMR spectra of synthetic compounds, in $CDCl_3$ or DMSO-d_6 with TMS as an internal standard. High-resolution mass spectra (HRMS) were recorded on a Shimazu LCMS-IT-TOF instrument with an ESI detector. All chemicals were purchased from commercial sources and all the solvents were of analytical reagents used without further purification. All oligonucleotides listed in Table S1 were purchased from Sangon Biotechnology Co., Ltd. (Shanghai, China), and G4 structures were pre-folded in 10 mM Tris-HCl buffer (containing 60 mM KCl, pH 7.4) unless otherwise noted and prepared as 100 μM stock solution, then their topological structures were confirmed by CD studies (Fig. S1).

2.2. Synthesis and characterization of synthesized compounds

2.2.1. Preparation of 9-(3-bromopropyl)-9H-carbazole (*1b*)

Under nitrogen atmosphere, sodium hydride (0.57 g, 23 mmol) was added to the mixed solution of carbazole (2 g, 12 mmol), DMF (2 mL) and THF (30 mL) stirred for 15 min at room temperature. Then 1,3-dibromopropane (3.6 g, 17.8 mmol) was blended into the reaction mixture and stirred at 50 °C for 5 h. After cooling, the organic phase was extracted with ethyl acetate (20 mL × 3) and purified by flash column chromatography with PE/EA = 40:1 elution to afford brown oily liquid **1b** (1.6 g, yield 47%). ^{1}H NMR (400 MHz, $CDCl_3$) δ 8.12 (d, J = 7.7 Hz, 2H), 7.55–7.45 (m, 4H), 7.3–7.22 (m, 2H), 4.52 (t, J = 6.5 Hz, 2H), 3.40 (t, J = 6.1 Hz, 2H), 2.47–2.44 (m, 2H).

2.2.2. Preparation of 9-(3-bromopropyl)-9H-carbazole-3-carbaldehyde (*1c*)

Phosphorus oxychloride (1.5 mL, 16 mmol) was mixed and dissolved in anhydrous DMF (5 mL) stirred at ice bath for 1 h. Intermediate **1b** (0.77 g, 2.7 mmol) dissolved in 1,2-dichloroethane was added into the reaction mixture at refluxed temperature for 12 h. After cooling to room temperature, the crude product was treated with saturated $NaHCO_3$ aqueous solution to reach the pH of 7.4 and extracted with dichloromethane (20 mL × 3). Then the combined organic phase was dried over anhydrous sodium sulfate and organic solvent was removed by rotary evaporation. The product was purified using flash silica gel column with PE/EA = 40:1 elution to afford faint yellow oily liquid **1c** (0.565 g, yield 68%).

2.2.3. Preparation of N-(pyridin-2-ylmethyl)ethanamine (*2c*)

2-pyridinecarboxaldehyde (0.5 g, 4.6 mmol) was added to a stirred solution of 2-picolylamine (0.5 g, 4.6 mmol) dissolved in methanol (50 mL) and stirred for 10 h under ambient temperature. The addition of sodium borohydride (0.7 g, 18.5 mmol) turned the reaction mixture from dark brown to pale yellow and stirred for another 2 h. All the volatiles were removed under reduced pressure and diluted hydrochloric acid was dropwise added to neutralize the alkalinity of excess sodium borohydride. After extraction by CH_2Cl_2 (20 mL × 3), the combined organic phase was dried over anhydrous sodium sulfate and the crude product was purified by aluminum trioxide column chromatography using DCM/MeOH = 20:1 as the eluent to obtain pure compound **2c** (0.18 g, yield 20%). ^{1}H NMR (400 MHz, $CDCl_3$) δ 8.53 (d, J = 8.4 Hz, 2H), 7.62 (t, J = 21.5, 10.8 Hz, 2H), 7.35 (d, J = 7.8 Hz, 2H), 7.14 (t, J = 15.7, 8.0 Hz, 2H), 3.98 (s, 4H), 2.84 (s, 1H).

2.2.4. Preparation of 9-(3-(bis(pyridin-2-ylmethyl)amino)propyl)-9H-carbazole-3-carbaldehyde (*3*)

565 mg (1.8 mmol) compound **1c** and 355 mg (1.8 mmol) compound **2c** were dissolved in 50 mL acetonitrile, the resultant mixture was refluxed at 80 °C for 12 h after the addition of anhydrous potassium carbonate (493 mg, 3.6 mmol). After cooling, small amount of water was added into the solution to dissolve potassium carbonate and the crude product was obtained by extraction with dichloromethane. With the completion of dryness over anhydrous sodium sulfate, pure compound **3** (464 mg, 60%) was afforded with aluminum trioxide column chromatography using DCM/MeOH = 30:1 as the eluent. ^{1}H NMR (400 MHz,

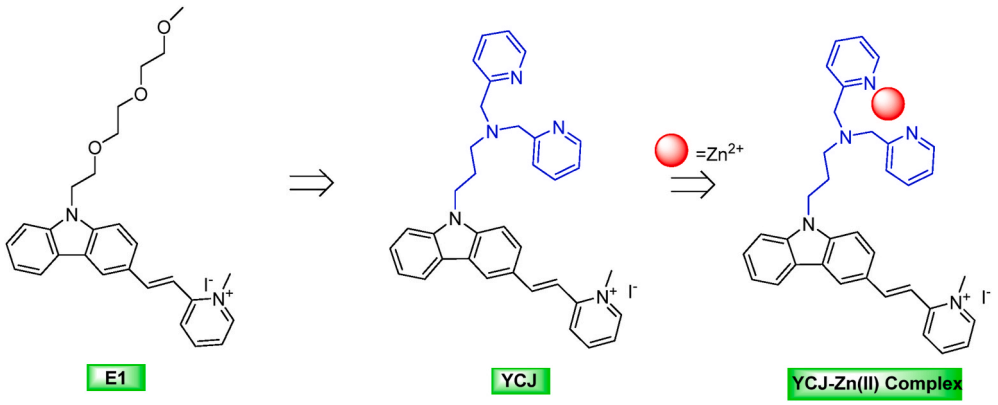

Fig. 1. Molecular structures of **E1**, **YCJ** and its Zn(II) complex.

$CDCl_3$) δ 10.05 (s, 1H), 8.58–8.48 (m, 3H), 8.10 (d, $J = 7.7$ Hz, 1H), 7.93 (d, $J = 8.5$, 1.5 Hz, 1H), 7.65–7.55 (m, 2H), 7.53–7.39 (m, 4H), 7.32–7.25 (m, 2H), 7.17–7.10 (m, 2H), 6.95 (d, $J = 11.2$ Hz, 4.6 Hz, 1H), 4.37–4.24 (m, 2H), 3.83 (s, 4H), 2.69 (t, $J = 6.9$ Hz, 2H), 2.14–2.01 (m, 2H).

2.2.5. Preparation of 2-(2-(9-(3-(bis(pyridin-2-ylmethyl)amino)propyl)-9H-carbazol-3-yl)vinyl)-1-methylpyridin-1-ium (YCJ)

A solution of **3** (464 mg, 1.1 mmol) in absolute ethyl alcohol (40 mL) was refluxed with 1,2-dimethylpyridin-1-ium iodide (251 mg, 1.06 mmol) along with a few drops of piperidine. After 4 h, the combined organic phase was concentrated under reduced pressure and pure product **YCJ** (110 mg, 20%) was obtained by recrystallization from DCM/MeOH. ^{1}H NMR (400 MHz, DMSO-d_6) δ 8.85 (d, $J = 6.1$ Hz, 1H), 8.70 (s, 1H), 8.54 (d, $J = 8.0$ Hz, 1H), 8.50–8.40 (m, 3H), 8.26–8.16 (m, 1H), 8.14 (s, 1H), 7.94 (dd, $J = 8.7$, 1.2 Hz, 1H), 7.81 (dd, $J = 10.1$, 3.7 Hz, 1H), 7.76–7.64 (m, 3H), 7.64–7.54 (m, 2H), 7.46 (t, $J = 8.4$ Hz, 3H), 7.32–7.17 (m, 3H), 4.41 (d, $J = 12.1$ Hz, 5H), 3.72 (s, 4H), 2.56 (t, $J = 6.7$ Hz, 2H), 2.00 (d, $J = 13.5$, 6.8 Hz, 2H) HRMS: (positive mode, m/z) calculated 524.2809, found 524.2814 for $[M - I]^+$.

2.3. Spectrophotometric and spectrofluorimetric titrations

UV–vis absorption studies were performed on UV-8000 spectrophotometer (Metash, China) using matched quartz cuvettes of 10 mm path length in 10 mM Tris-HCl (60 mM KCl) buffer. Fluorescence titration studies were performed on RF-5301PC fluorescence spectrophotometer (Shimazu, Japan) with 10 mm quartz cuvettes in which fluorescence was measured in 10 mM Tris-HCl (60 mM KCl) buffer and the spectra were recorded at 2 nm excitation and emission slit widths unless otherwise specified. The fluorescence excitation wavelength was set as 419 nm and emission was ranged from 420 to 700 nm. For the titration test both in spectrophotometry and spectrofluorimetry, the concentration of stock solution was constant while different DNA solutions were added step by step until no change was observed in the spectra, indicating that binding saturation was achieved.

2.4. CD spectra measurement

CD spectra titration was performed by using a JASCO J-815 CD spectrometer continuously flushed with pure evaporated nitrogen throughout the experiment. The concentration of *c-myc* DNA was fixed at 2 μM while the incremental amount of *in situ* generated **YCJ-Zn(II)** ensemble from 2 μM to 20 μM was added into the Tris-HCl buffer containing *c-myc* DNA. The spectra were accumulated over the wavelength range of 230–320 nm with a bandwidth of 1.0 nm and 60 nm/min scanning speed. After each addition of compound, the mixed solution was vibrated adequately and equilibrated at least 2 min before scan. The data of Tris-HCl buffer as a background baseline had been subtracted from each sample at the beginning of titration.

2.5. Molecular docking

Docking analysis was carried out by using the Autodock 1.5.6 modeling tool. The crystal structure of *c-myc* G4 (PDB ID:1XAV) was downloaded from RCSB PDB nucleic acid database. And all of the water molecules and metal ions were extracted from the maternal structure of nucleic acid 1XAV and all of the hydrogen atoms (including polar and nonpolar hydrogen atoms) were added to define the correct configurations and tautomeric states. The ligand was converted from a two-dimensional structure into three-dimensional structure using ChemDraw 3D with minimized energy. The grid box dimension was determined by visual inspection to encompass the whole G 4 structure but also left additional space for maximum flexibility in ligand orientation. All of the possible docking sites recommended by docking-scoring analysis were displayed by PyMOL 1.7.6 software for visualizing covalent and non-covalent interactions between ligand and acceptor 1XAV nucleic acid.

2.6. Cell staining experiments

4T1 cells were grown in DMEM medium with fetal bovine serum (10%). For the localization study, cells were cultured in confocal dishes at 37 °C for 24 h first. After the cells were washed twice with PBS, 20 μM *in situ* generated **YCJ-Zn(II)** ensemble was added. After the cells were cultured at 37 °C for 30 min, the medium was removed, and the cells were further incubated with 1.0 μg/mL DAPI for 30 min at 37 °C. After the cells were washed three times with PBS, the images were processed.

2.7. DNase and RNase digest test

4T1 cells were cultured in confocal dishes for 24 h. Then, the cells were fixed by precooled methanol for 15 min. After being washed twice with PBS, the cells were treated with Triton X-100 (1%) for 2 min. After being washed twice with PBS, the pretreated cells were incubated with **YCJ-Zn(II)** ensemble or DAPI, respectively for 1 h at 37 °C. After the cells were washed three times with PBS, one dish was used as a blank, and the other dishes were respectively treated with DNase (RNase-free, 30 μg/mL) or RNase (30 μg/mL) at 37 °C for 2 h. Cells were rinsed by PBS three times before imaging.

3. Results and discussion

3.1. Chemistry

With the aim to increase the binding affinity and the biocompatibility of probe **E1**, we decorated carbazole-pyridinium scaffold with DPA substituent *via* different alkyl linker to afford ligand **YCJ**. As was outlined in Scheme 1, in the first step, the commercially available carbazole was reacted with 1,3-dibromopropane under inorganic basic condition to afford 9-(3-bromopropyl)-9H-carbazole (**1b**). The intermediate **1b** was then treated with phosphonium oxychloride ($POCl_3$) in DMF under heating condition to obtain 9-(3-bromopropyl)-9H-carbazole-3-carbaldehyde (**1c**). In the second step, treating pyridine-2-carboxaldehyde with 2-aminopyridine and sodium borohydride led to the formation of 2,2′-dipicolylamine (DPA), which was subsequent reacted with compound **1c** to give the intermediate **3**. Finally, knoevenagel condensation of intermediate **3** with pyridinium in the presence of organic base in anhydrous ethanol led to afford desired ligand **YCJ** as a yellow solid. Experimental data including ^{1}H NMR, ^{13}C NMR and high-resolution mass spectrometry supported their structures (see the Supplementary Information).

3.2. Fluorescence response towards c-myc G4 DNA

Previously, when the probe **E1** was used to interact with *c-myc* G4 DNA, the observed fluorescence enhancement was only about 8-fold, that is, the fluorescence response is relatively low toward G4 DNA. In order to investigate the ability of this new ligand in the fluorescence detection of G4 DNA, the fluorescence response of **YCJ** toward *c-myc* G4 DNA in the presence of Zn(II) was first studied. The ligand **YCJ** exhibits a weak fluorescence signal in buffer solution with $\lambda_{max} = 544$ nm upon excitation at 419 nm. When combined with Zn(II), a little decrease was observed in the fluorescence (Fig. S2). The job plot shows the formation of a 1:1 bonding mode between **YCJ** and Zn (II) (Fig. S3). To get further insight into the binding mode of **YCJ** and Zn^{2+}, the ^{1}H NMR analysis of ligand **YCJ** in DMSO-d_6 in the presence of 1.0 equiv. of Zn^{2+} was recorded and the result was shown in Fig. S4. The protons at pyridine were all broadened and downfield shifted upon addition of Zn^{2+}. Meanwhile, the singlet peak of methylene protons in DPA moiety at 3.72 ppm was shifted downfield to 4.13 ppm. Accordingly, the structure of YCJ-Zn^{2+} was proposed in Fig. S4, in which Zn^{2+} may coordinate with

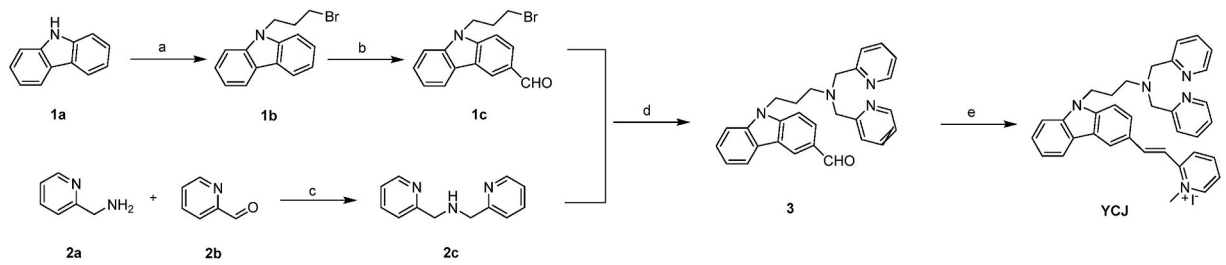

Scheme 1. Synthetic routes for the preparation of ligand **YCJ**. Reagents and conditions: a.1,3-dibromopropane, NaH, DMF, THF, rt, 5 h; b. DMF, $POCl_3$, 80 °C; c. $NaBH_4$, MeOH, rt, 10 h; d.K_2CO_3, acetonitrile, reflux,12h; e. Piperidine, EtOH, reflux, 12 h.

DPA nitrogen atoms. The observed spectral behavior of **YCJ-Zn(II)** complex is particularly interesting from the perspective of an ideal fluorescence probe that is almost non-fluorescence in free-state and strongly intensity in the analyte bound-state. On the basis of this result, quantitative analysis of the *in situ* generated **YCJ-Zn(II)** ensemble toward *c-myc* G4 DNA was investigated by fluorescent titration in Tris-HCl buffer (pH 7.4, containing 60 mM KCl). As shown in Fig. 2A, when *c-myc* G4 DNA was gradually added, there was a large fluorescence enhancement at λ = 544 nm. Fig. 2B compares the fluorescence responses of E1 and YCJ-Zn(II) complex with *c-myc* G4 DNA, which demonstrates this complex gives much better performance than its precursor E1. Additionally, according to the titration curve, a linear correction between fluorescence intensity of YCJ-Zn(II) complex and the concentration of *c-myc* G4 DNA in the range of 0.2–1.6 μM was observed with $R^2 = 0.991$ (Fig. 2C). The limit of detection (LOD) was calculated to be as low as 68 nM according to the IUPAC-based method [37]. The LOD value of YCJ-Zn(II) complex for *c-myc* G4 DNA in solution is significantly improved relative to ligand E1 (LOD = 160 nM). The above fluorescence measurement demonstrates that the YCJ-Zn(II) complex displays greatly enhanced fluorescence performance over ligand E1 in the detection of *c-myc* G4 DNA. It has initially validated our proposed idea.

Combining with the study on E1, the strong fluorescence enhancement of YCJ-Zn(II) complex originates from the restriction of rotation around the vinylic-bridge upon its G4 binding, which is also illustrated by the emission enhancement in a viscous medium (Fig. S5). Commonly, fluorescent molecular rotors usually show longer fluorescence lifetimes in a restricted environment. Fluorescence intensity decay measurements were then conducted to demonstrate the binding of YCJ-Zn(II) complex with *c-myc* G4 DNA (Fig. 2D). The normalized fluorescence decay data of free YCJ-Zn(II) complex and *c-myc* G4 DNA bound YCJ-Zn(II) complex has been shown in a scatter plot and typical decay profiles along with autocorrelation diagrams are shown in Fig. 2D. The decays were fitted with a three-exponential function. The major decay component (34%) had a lifetime of 2.1 ns for G4 DNA bound YCJ-Zn(II) complex, and the other two decays (2.3 ns and 7.2 ns) had an amplitude of 58%. The average fluorescence lifetime of 4.71 ns was calculated from the above three exponentials, which was 4 times the 1.10 ns of free YCJ-Zn(II) complex. This result indicates that the strong interaction between YCJ-Zn(II) complex and *c-myc* G4 DNA hinders the molecular rotation and increases its lifetime.

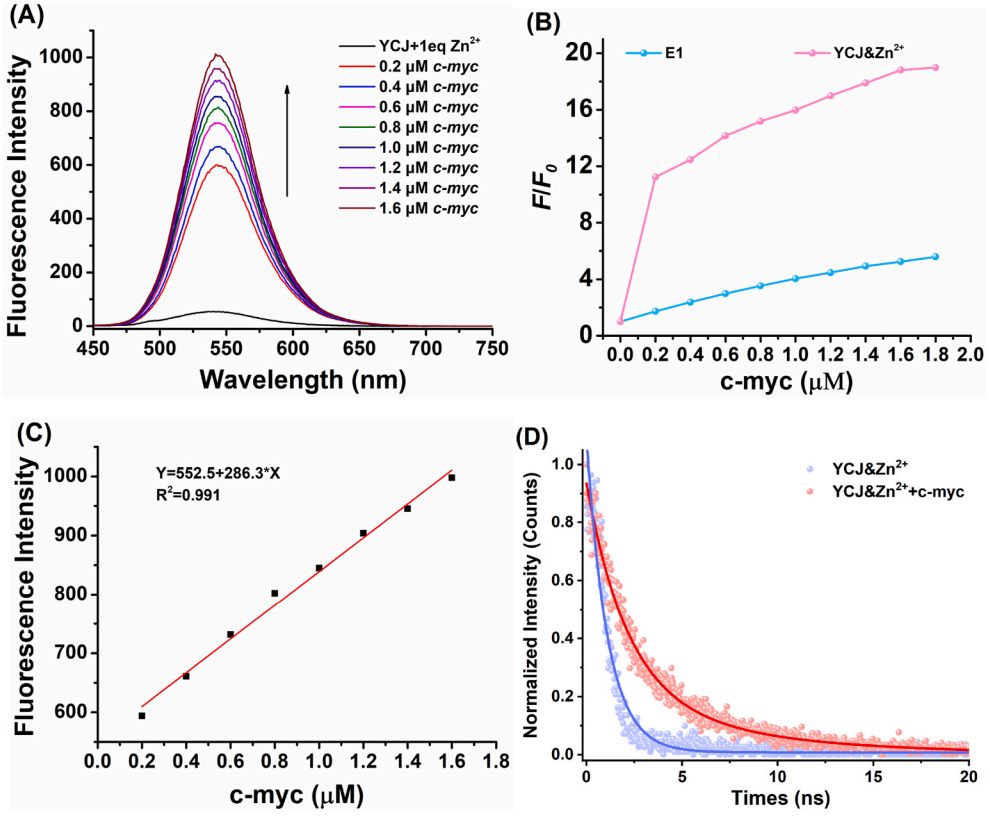

Fig. 2. (A) Fluorescence titration spectra of **YCJ** (1 μM) + 1 eq Zn^{2+} with the addition of *c-myc* from 0.2 to 1.6 μM in 10 mM Tris-HCl buffer, 60 mM KCl, pH 7.4. **(B)** Intensity ratio change of **E1** and **YCJ-Zn(II) complex** (1 μM) with the addition of c-myc from 0.2 to 1.8 μM in buffered solution. **(C)** The linear fit equation for calculating LOD value between **YCJ-Zn(II)** complex and *c-myc* G4 DNA at 545 nm. **(D)** Fluorescence lifetime decay of **YCJ-Zn(II)** complex with/without *c-myc* in 10 mM Tris-HCl buffer, 60 mM KCl, pH 7.4.

3.3. Selectivity study of *YCJ-Zn(II)* complex towards G4 DNAs against other DNA forms

We then studied the fluorescence responses of **YCJ** in combination with Zn(II) towards other G4s (22AG, EAD, G3T3, HT, Htg-21, Hum24, Pu27, VEGF, ODN, CM22), double-stranded DNAs (dsDNA26, $(A\text{-}T)_2$, $(A\text{-}T)_5$, $(A\text{-}T)_9$, $(G\text{-}C)_9$), and single-stranded DNA (ss26) (Fig. S6). The titration curves manifest that the fluorescence enhancements at 544 nm are increased to different extents and depend on the types of DNA. Notably, G4s could significantly enhance the fluorescence signal of **YCJ-Zn(II)** complex (12- to 20-fold). Only weak fluorescence enhancements are observed upon binding to single-stranded and double-stranded DNAs (less than 5-fold). The results are summarized in Fig. 3. Thus, these results show that **YCJ-Zn(II)** complex preferentially recognizes G4 DNA in vitro.

3.4. Binding characteristics

Electronic absorption spectroscopy is a sensitive method for determining the binding characteristics of small organic molecules and/or their metal complexes with G4 DNA. Changes observed in the electronic absorption spectrum reflect the interaction between the molecules of a particular compound/complex and DNA, and inferences may be drawn regarding the mechanism of this interaction from wavelength shifts of the corresponding absorption bands. In our experiments, we investigated the effect of adding *c-myc* G4 DNA to a solution of **YCJ-Zn(II)** complex. For comparison, the absorption spectrum of **E1** in the presence of *c-myc* G4 DNA was also collected. In the case of **E1**, as shown in Fig. 4A, hypochromicity of 54.4% and small bathochromic shift of 5 nm are observed. Addition of the *c-myc* G4 DNA to the **YCJ-Zn(II)** complex has led to a 33.9% decrease in intensity and a large red shift of 32 nm in the absorption spectra as shown in Fig. **4B**. Generally, bathochromism can be explained on the basis of the coupling of an antibonding π^* orbital of the intercalating ligand and the π-orbital of the DNA base pairs, which thus lowers the $\pi \rightarrow \pi^*$ transition energy, and in turn results in a shift to longer wavelengths [38]. Given that the coupled π orbital is not fully filled with electrons, there is a decrease in the values of the spectral transition probabilities and this is reflected in the spectrum as a decrease in absorbance (hypochromism) [39,40]. In other words, hypochromism is indicative of intercalative binding whereas the bathrochromic shift is an indication of strong stacking interaction between the ligand chromophore and bases of DNA. Comparing the data on the bathochromic shift and hypochromic effect, it can be assumed that **YCJ-Zn(II)** complex may be bound through strong stacking interactions to the *c-myc* G4 DNA structure. Coordination of Zn(II) to aromatic ligand may decrease the ligand's electron density and consequently enhance the ability to display π-π stacking interactions with G4 DNA, which resulted in larger extent of bathochromism.

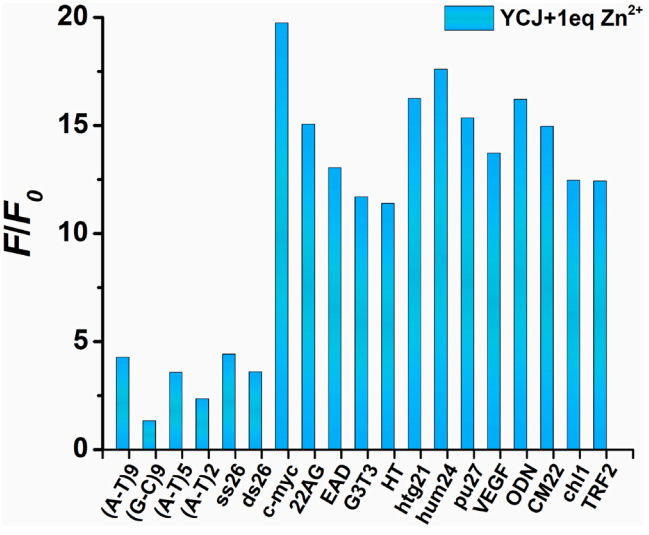

Fig. 3. Distribution for the values of F/F_0 of **YCJ-Zn(II) complex** for all the tested oligonucleotides at the saturated concentration in 10 mM Tris-HCl buffer, 60 mM KCl, pH 7.4.

3.5. The effect of *YCJ- Zn(II) complex* on the conformation and stability of c-myc G4 DNA

To gain insights into the binding event, highlighting the effect of the complex on the conformation of *c-myc* G4 DNA structure, circular dichroism (CD) experiment was conducted. The CD spectrum of the pre-folded *c-myc* alone in a buffer containing 60 mM KCl and 10 mM Tris-HCl at pH 7.4 shows the characteristic signature reported in the literature for this sequence, displaying a maximum at 260 nm and a negative at 245 nm, corresponding to the parallel G4 structure [41]. After addition of **YCJ-Zn(II)** complex, a slight dropping of the intensity of the positive band at 260 nm, an increase of the negative band at 245 nm was observed (Fig. 5). Since the G4 structure might be affected by metal ions, a CD titration of pure Zn(II) into the solution of *c-myc* G4 DNA under the same conditions was also conducted. As seen in Fig. S7, it had almost no effect on the CD intensity, indicating that Zn(II) would not affect the *c-myc* G4 DNA structure. In general, addition of **YCJ-Zn(II)** complex does not affect the positions of peaks, suggesting that the G4 structure retained the parallel topology. A gradual decrease in the intensity of CD signal suggests more or less perturbation in the perfect stacking between tetrads in the G4 DNA by **YCJ-Zn(II)** complex. This finding is also consistent with the UV–vis signal observed in the absorption titration experiment.

3.6. Study on the binding mechanism of *YCJ-Zn(II) complex* with c-myc G4 DNA

The above experimental results show that the probe **YCJ-Zn(II)** complex is giving more effective fluorescent signal discrimination to G4 DNA. The enhanced fluorescence signal may also reveal that the molecular rotating ability may be effectively restricted because the molecular size of the complex is small enough to fit into the G4-binding pocket. The favorable adduct may probably form through the π-π stacking interactions between the planner carbazole and G4-structure. Next, the binding stoichiometry of **YCJ-Zn(II)**/*c-myc* complex in solution was assessed by using Job's plot method, in which the maximum fluorescence intensity peaked at about 0.67 fraction of **YCJ-Zn(II)**, indicated that a 2:1 complex was formed (Fig. S8). In order to comprehensively understand the nature of interaction and binding mode between **YCJ-Zn(II)** complex and G4 DNA, an elementary and rapid technique, fluorescent intercalator displacement (FID) assay, was exploited in this study. This assay is based on the displacement of an "on/of" fluorescence probe **YCJ-Zn(II)** complex from G4 DNA matrices by increasing amounts of a putative G4 binder hemin which considered as binding to G4 DNA through both 5′ and 3′ end-stacking modes by forming a 2:1 (hemin/G4) complex [42]. If hemin has the same binding site as **YCJ-Zn(II)** complex, will compete with **YCJ-Zn(II)** complex for G4 DNA binding, resulting in the large decrease of the emission. As illustrated in Fig. S9, the displacement with hemin induced almost fully quenched in the fluorescence intensity of **YCJ-Zn(II)**/*c-myc* complex. The result clearly indicates that **YCJ-Zn(II)** complex binds to G4 DNA with the same site as hemin.

To verify whether the binding site of **YCJ-Zn(II)** complex to *c-myc* G4 DNA was at the 3′ or 5′ terminal, we monitored the impact of **YCJ-Zn(II)** complex binding on the modified *c-myc* G4 DNA with aminomethylcoumarin (AMCA) substituted at position of 3′ and 5′-terminus of the *c-myc* sequence. Theoretically, at which end **YCJ-Zn(II)** complex bound, the AMCA fluorescence will be quenched Fig. 6. It was found that the fluorescence intensities of 5′ and 3′-labeled *c-myc* G4 DNA were

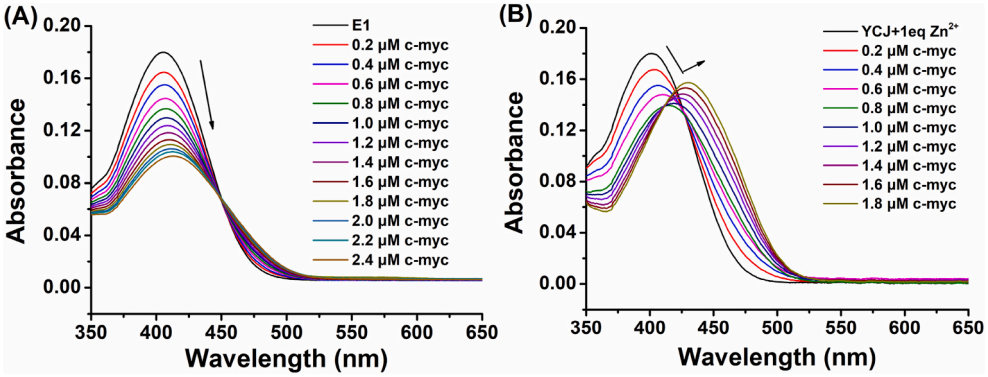

Fig. 4. UV–vis spectra for titrations of *c-myc* stepwise to **(A) E1** and **(B) YCJ-Zn(II)** complex (5 μM) in 10 mM Tris-HCl buffer, 60 mM KCl, pH 7.4. The spectra were recorded at 2 min intervals.

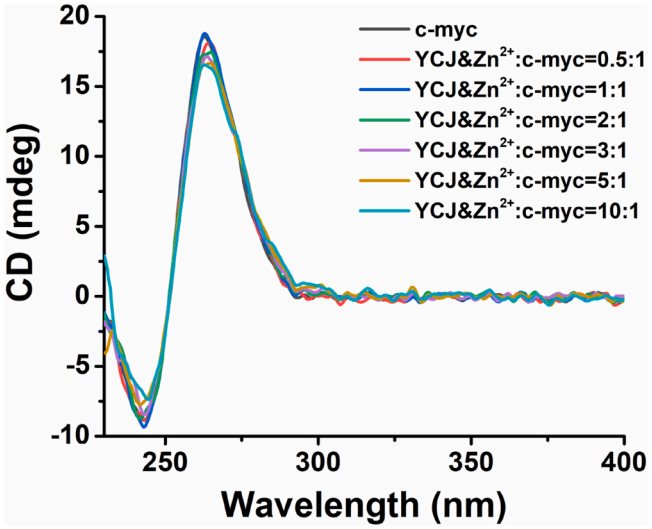

Fig. 5. CD titration spectra of *c-myc* G4 DNA (2 μM) with 0–10 equiv **YCJ-Zn (II)** complex in 10 mM Tris-HCl buffer, 60 mM KCl, pH 7.4.

significantly disturbed upon the addition of **YCJ-Zn(II)** complex, indicating that **YCJ-Zn(II)** complex had close contact with these regions. In other words, both 3′ and 5′-ends of G4 DNA may be the binding sites for **YCJ-Zn(II)** complex.

Because loops are distributed on the side faces of parallel *c-myc* G4 DNA, the side arms on the carbazole core may approach the groove and loop regions and interact with them. To further gain insight into the additional binding sites, several mutated *c-myc* G4 DNA sequences with extension or shortening the length of different loops were prepared. CD spectroscopy confirms that these mutated *c-myc* DNA sequences do not disturb the parallel G4 conformation (Fig. S10). The changes of their fluorescence emission spectra and fluorescence intensity were observed and recorded (Table 1). **The elongation or shortening of the loop near 5' end has almost no effect on fluorescence intensity, while other loops have a little effect on the enhancement of fluorescence that compared with original *c-myc* G4 DNA. The above results suggest that YCJ-Zn(II) complex targets the *c-myc* G4 DNA mainly by end-stacking mode, and partially by groove/loop mode.**

Molecular docking is proven to be an important technique, useful to predict the interaction of small ligands with biological macromolecules. Ligand YCJ and its Zn(II) complex were introduced in the docking analysis to further clarify detail DNA interactions toward *c-myc* G4 DNA (PDB:1XAV) using Autodock Vina software [43]. The best favorable binding poses were selected from the docking results as depicted in Figs. 7 and S11, and their binding energies were calculated (Table 2). It

Table 1
Relative fluorescence intensities of YCJ-Zn(II) complex (1 μM) in the presence of *c-myc* G4s (2 μM) with different flanking loops in 10 mM Tris-HCl buffer, 60 mM KCl, pH **7.4.**

Name	Sequence (5′-3′)	Relative FI
c-myc	TTGA GGG T GGG TA GGG T GGG TAAA	1000
c-myc-A	TTGA GGG T AAA GGG TA GGG T GGG TAAA	1000
c-myc-B	TTGA GGG T GGG TAATT GGG T GGG TAAA	704
c-myc-C	TTGA GGG T GGG TA GGG TAAT GGG TAAA	658
c-myc-D	TTGA GGG T GGG T GGG T GGG TAAA	641
c-myc-E	TTGA GGG T GGG TA GGG TA GGG TAAA	816

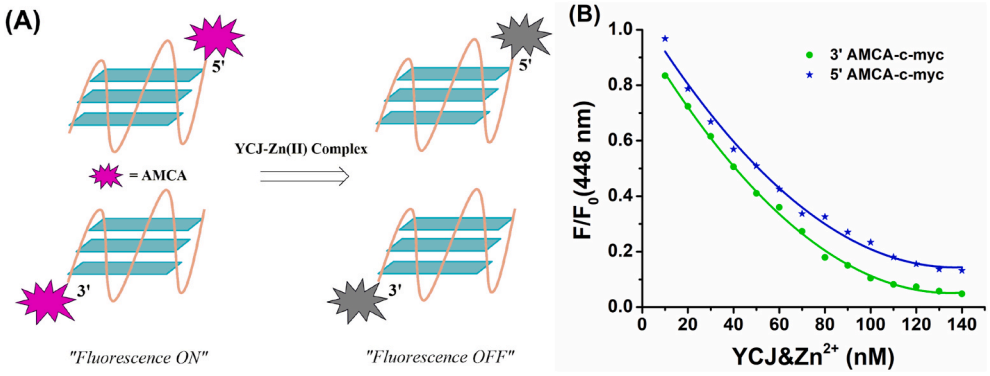

Fig. 6. (A) Schematic representation of AMCA (aminomethylcoumarin) modified G-quartet regulated by **YCJ-Zn(II)** complex. **(B)** The ratio (F/F_0) of fluorescence intensity of 5'/3′ AMCA-labeled *c-myc* G4 (0.2 μM) with the addition of **YCJ-Zn(II)** complex in 10 mM Tris-HCl buffer, 60 mM KCl, pH 7.4. λ_{ex} = 353 nm and λ_{em} = 448 nm.

has been previously shown that G4 binders contain a planar π-aromatic surface can stack on the surface of both terminal G-quartet planes. Here, both of them were found to stack in the centers of 3′ and 5′-terminals. When the ligand YCJ binds to at 5′-terminal, the two benzene rings of carbazole have π-π stacking interactions with DG-10 and DG-15 respectively, and CH-π stacking also occurred between the vinyl group in the pendant chain and DG-10 base. In addition, one of the pyridine rings of DPA moiety was encapsulated by a hydrophobic cavity composed of DG-9, DG-10, DA-12, and DG-14. After DPA moiety chelated with zinc ion, it had the propensity to be closer to the central ion channel that is negatively charged in the center of G-tetrad due to electrostatic interactions, and divalent zinc ion exhibited cation-π interaction with DG-15. Besides, a hydrophobic cavity composed of DG-10, DA-12, DG-9, DG-14, and DG-13 wrapped the pyridine group connected by the vinyl bond. It is noteworthy that the lower binding free energy of YCJ-Zn(II) complex also suggests more favorable binding interactions with G4 DNA than its metal-free ligand due to the expected electrostatic interactions. Similar results were found with the 3′-terminal binding process. They indicated that introducing metal ions in the ligand could create some interesting differences in the DNA binding properties, therefore, such structural information of the complex is important for designing new G4 probes with enhanced binding activity.

3.7. Confocal fluorescence imaging

Following consideration of above properties of YCJ-Zn(II) complex, we further studied its biological application in cell imaging Fig. 8 presented the fluorescence images of 4T1 cells stained with YCJ-Zn(II) complex directly or after deoxyribouclease (DNase) and ribonuclease (RNase) treatments. The localization in cells was illustrated through co-staining with the nucleus-targeted dye DAPI. Apparently, the DAPI dye brightened up the whole nucleus with blue-emitting. The 4T1 cells after treated with YCJ-Zn(II) complex showed intensive green fluorescence signal in the nucleolus region. Compared with our previous reported probe E1 that localized in the cytoplasm with weak fluorescence signal, the results suggested that Zn(II)-DPA moiety could enhance the ability for penetration through the nuclear membrane. To verify the binding target of YCJ-Zn(II) complex in nucleoli, enzymes DNase and RNase digest experiments were conducted. As shown in Fig. 8, the produced green fluorescence signals of YCJ-Zn(II) complex in nucleus clearly disappeared after DNase treatment but did not affect by RNase,

Table 2
Estimated free energy of binding (ΔG, kcal·mol^{-1}) for G4 DNA.

Compound	5′ terminus	3′ terminus
YCJ5	−6.1	−7.8
YCJ5-Zn(II) complex	−9.0	−9.2

suggesting that YCJ-Zn(II) complex interacted with endogenous DNA in cells. The nucleolus is an organelle where rDNA undergoes transcription to rRNA, and G-rich double strands can separate into single-strand DNA which may transitorily fold into G4s during transcription and replication. Although YCJ-Zn(II) complex exhibited selectivity towards G4 DNAs in vitro experiments, the selectivity in vivo was insufficient. The co-staining experiment results revealed that the abundant presence of duplex DNA in the nucleus is expected to play important role in the fluorescence enhancement of YCJ-Zn(II) complex due to non-specific binding to duplex DNA. Therefore, the strong green fluorescence of YCJ-Zn(II) complex was induced within almost the whole nucleus. The clear staining images demonstrated that YCJ-Zn(II) complex was suitable for monitoring of nucleus activities.

4. Conclusions

Metal complexes have been considered as an emerging class of compounds targeting G4 DNA. To uncover the important structural determinants contributing to the improvement of effective G4 DNA probes, we have prepared a ligand YCJ based on the promising structure of the previously discovered G4 DNA probe E1, which covalently linking a metal ion chelator DPA and a carbazole-pyridinium scaffold. This ligand in combination with Zn(II) has exhibited affinity toward G4 DNA with promising fluorescence intensity enhancement and red-shift in absorption spectra. To characterize in more detail the interaction between this complex and G4 DNA, comprehensive studies were carried out with *c-myc* DNA as a representative example of a G4 structure. It is proposed that the Zn-coordination could significantly enhance G4 DNA binding affinity and cellular uptake. We expect that this research would help to guide the development of high performance metal complex as G4 DNA probes with higher binding affinity, improved biocompatibility and enhanced functional properties to monitor and study in live cells.

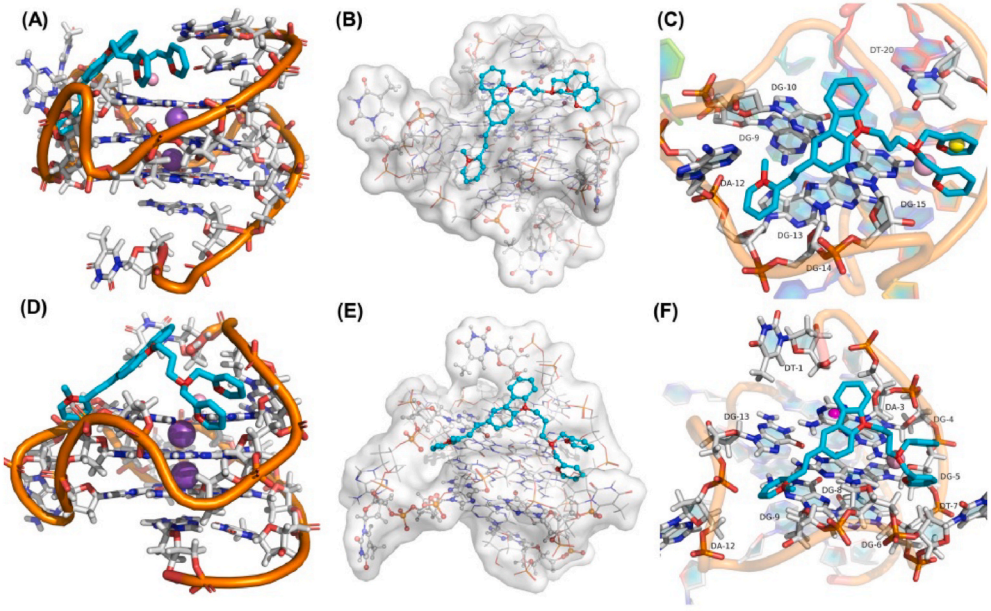

Fig. 7. Structure of ligand YCJ-Zn(II) complex with G4 DNA at the 3′ terminal (A–C) and 5′ terminal (D–F), derived from NMR (PDB:1XAV). (A)(D) Metal potassium ions used to stabilize the G4 structure were represented by purple spheres. Guanine bases that make up for G-tetrad and bases in the loop region were shown in the stick model. Carbon atoms on benzene ring and alkane chain were displayed by cyan color stick, nitrogen atoms in tv-red color and zinc ion in pink sphere. Non-covalent interactions including hydrogen bond, π-π stacking, CH-π and cation-π interactions were shown in dotted line. Figs were rendered using PyMOL. (For interpretation of the references to color in this figure legend, the reader is referred to the Web version of this article.)

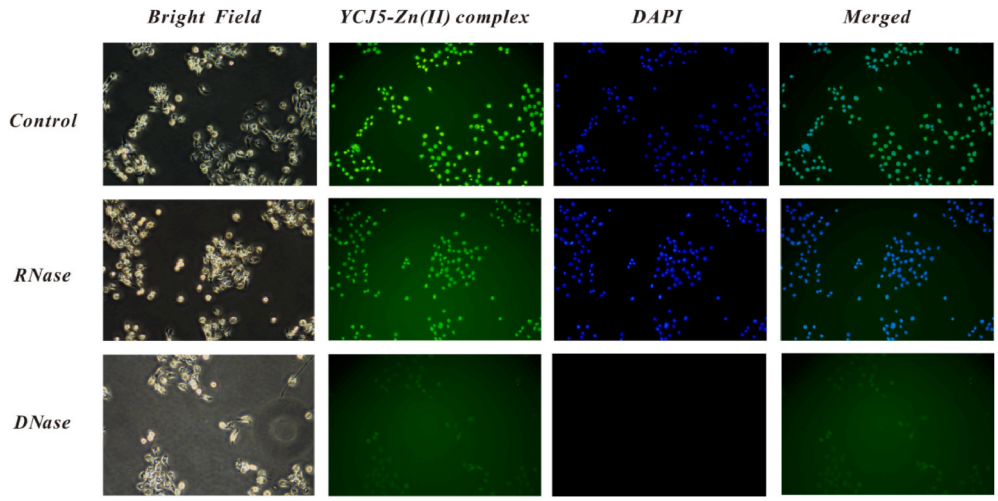

Fig. 8. Fluorescence images of 4T1 cells stained with 20 μM of YCJ-Zn(II) complex for 30 min and 1.0 μg/mL DAPI for 30 min without and with DNase or RNase treatment. The cells were excited and imaged by using a confocal fluorescence microscope within the given range of wavelengths pass through 335–385 nm for DAPI and 465–496 for YCJ-Zn (II) complex.

CRediT authorship contribution statement

Quan-Qi Yu: Conceptualization, Methodology, Data curation. **Xue-Xian Lang:** Methodology. **Juan-Juan Gao:** Methodology. **Hong-Yao Li:** Data curation. **Yi-Tong Bai:** Data curation. **Hai-Jiao Wang:** Conceptualization, Methodology. **Ming-Qi Wang:** Supervision, Conceptualization, Writing – review & editing.

Declaration of competing interest

The authors declare that they have no known competing financial interests or personal relationships that could have appeared to influence the work reported in this paper.

Acknowledgements

This work was financially supported by the National Natural Science Foundation of China (21907042), Natural Science Foundation of Jiangsu Province (BK20180857), The Key Scientific Research Project of Colleges and Universities in Henan Province (20A150034).

Appendix B. Supplementary data

Supplementary data to this article can be found online at https://doi.org/10.1016/j.dyepig.2021.109707.

References

[1] Gellert M, Lipsett MN, Davies DR. Helix formation by guanylic acid. Proc Natl Acad Sci USA 1962;48:2013–8.
[2] Burge S, Parkinson GN, Hazel P, Todd AK, Neidle S. Quadruplex DNA: sequence, topology and structure. Nucleic Acids Res 2006;34(19):5402–15.
[3] Chambers VS, Marsico G, Boutell JM, Di Antonio M, Smith GP, Balasubramanian S. High-throughput sequencing of DNA G-quadruplex structures in the human genome. Nat Biotechnol 2015;33(8):877–81.
[4] Marsico G, Chambers VS, Sahakyan AB, McCauley P, Boutell JM, Di Antonio M, Balasubramanian S. Whole genome experimental maps of DNA G-quadruplexes in multiple species. Nucleic Acids Res 2019;47(8):3862–74.
[5] Huppert JL, Balasubramanian S. Prevalence of quadruplexes in the human genome. Nucleic Acids Res 2005;33(9):2908–16.
[6] Kosiol N, Juranek S, Brossart P, Heine A, Paeschke K, G-quadruplexes. A promising target for cancer therapy. Mol Canc 2021;20:1–18.
[7] Do NQ, Chung WJ, Truong THA, Heddi B, Phan AT. G-quadruplex structure of an anti-proliferative DNA sequence. Nucleic Acids Res 2017;45:7487–93.
[8] Hänsel-Hertsch R, Spiegel J, Marsico G, Tannahill D, Balasubramanian S. Genome-wide mapping of endogenous G-quadruplex DNA structures by chromatin immunoprecipitation and high-throughput sequencing. Nat Protoc 2018;13:551–64.
[9] Biffi G, Tannahill D, McCafferty J, Balasubramanian S. Quantitative visualization of DNA G-quadruplex structures in human cells. Nat Chem 2013;5(3):182–6.
[10] De Magis A, Manzo SG, Russo M, Marinello J, Morigi R, Sordet O, Capranico G. DNA damage and genome instability by G-quadruplex ligands are mediated by R loops in human cancer cells. Proc Natl Acad Sci USA 2019;116:816–25.
[11] Rodriguez R, Miller KMK, Forment JV, Bradshaw CR, Nikan M, Britton S, Oelschlaegel T, Xhemalce B, Balasubramanian S, Jackson SP. Small molecule-induced DNA damage identifies alternative DNA structures in human genes. Nat Chem Biol 2012;8:301–10.
[12] Hänsel-Hertsch R, Simeone A, Shea A, Hui WWI, Zyner KG, Marsico G, Rueda OM, Bruna A, Martin A, Zhang X, Adhikari S, Tannahill D, Caldas C, Balasubramanian S. Landscape of G-quadruplex DNA structural regions in breast cancer. Nat Genet 2020;52(9):878–83.
[13] Ghuman A, Kavalukas S, Sharp SP, Wexner SD. Clinical role of fluorescence imaging in colorectal surgery-an updated review. Expet Rev Med Dev 2020;17(12):1277–83.
[14] Ma DL, Wang M, Lin S, Han QB, Leung CH. Recent development of G-quadruplex probes for cellular imaging. Curr Top Med Chem 2015;15:1957–63.
[15] Suseela YV, Narayanaswamy N, Pratihar S, Govindaraju T. Far-red fluorescent probes for canonical and noncanonical nucleic acid structures: current progress and future implications. Chem Soc Rev 2018;47:1098–131.
[16] Bhasikuttan AC, Mohanty J. Targeting G-quadruplex structures with extrinsic fluorogenic dyes: promising fluorescence sensors. Chem Comm 2015;51:7581–97.
[17] Vummidi BR, Alzeer J, Luedtke NW. Fluorescent probes for G-quadruplex structures. Chembiochem 2013;14:540–58.
[18] Dhamodharan V, Pradeepkumar PI. Specific recognition of promoter G-quadruplex DNAs by small molecule ligands and light-up probes. ACS Chem Biol 2019;14:2102–14.
[19] Leczkowska A, Gonzalez-Garcia J, Perez-Arnaiz C, Garcia B, White AJP, Vilar R. Binding studies of metal-salphen and metal-bipyridine complexes towards G-quadruplex DNA. Chem-A Eur J 2018;24(45):11785–94.
[20] Georgiades SN, Abd Karim NH, Suntharalingam K, Vilar R. Interaction of metal complexes with G-quadruplex DNA. Angew Chem Int Ed 2010;49(24):4020–34.
[21] Xu CX, Liu LY, Lv B, Zhao HY, Cao Q, Zhai T, Mao ZW. Two novel fan-shaped trinuclear Pt(ii) complexes act as G-quadruplex binders and telomerase inhibitors. Dalton Trans 2020;49(27):9322–9.
[22] Liu XW, Liu NY, Deng YQ, Wang S, Liu T, Tang YC, Chen YD, Lu JL. A luminescence probe for c-myc G-quadruplex by a triphenylamine-appended ruthenium complex. Appl Organomet Chem 2021:e614.
[23] Kench T, Vilar R. Metal complexes as G-quadruplex binders. Annu Rep Med Chem 2020;54:485–515.
[24] Tan CP, Zhong YM, Ji LN, Mao ZW. Phosphorescent metal complexes as theranostic anticancer agents: combining imaging and therapy in a single molecule. Chem Sci 2021;12(7):2357–67.
[25] Xie JE, Luo YH, Zhang QL, Zhang PY. Metal complexes in application of two-photon luminescence probes. Prog Chem 2021;33(1):111–23.
[26] Cao Q, Li Y, Freisinger E, Qin PZ, Sigel RKO, Mao ZW. G-quadruplex DNA targeted metal complexes acting as potential anticancer drugs. Inorg Chem Front 2017;4(1):10–32.
[27] Bononi G, Iacopini D, Cicio G, Di Pietro S, Granchi C, Di Bussolo V, Minutolo F. Glycoconjugated metal complexes as cancer diagnostic and therapeutic agents. ChemMedChem 2021;16(1):30–64.
[28] Cho SW, Rao AS, Bhunia S, Reo YJ, Singha S, Ahn KH. Ratiometric fluorescence detection of Cu(II) with a keto-dipicolylamine ligand: a mechanistic implication. Sens Actuators, B 2019;279:204–12.
[29] Peng X, Du J, Fan J, Wang J, Wu Y, Zhao J, Sun S, Xu T. A selective fluorescent sensor for imaging Cd2+ in living cells. J Am Chem Soc 2008;129(6):1500–1.

[30] Ballesteros E, Gómez DT, Rodríguez T, Rojo J, García-Valverde M, Torroba T. A new selective chromogenic and turn-on fluorogenic probe for copper(II) in Water–Acetonitrile 1:1 solution. Org Lett 2009;11(6):1269–72.
[31] Wong BA, Friedle S, Lippard SJ. Solution and fluorescence properties of symmetric dipicolylamine-containing dichlorofluorescein-based Zn2+ sensors. J Am Chem Soc 2009;131(20):7142–52.
[32] Roy B, Rao AS, Ahn KH. Mononuclear Zn(II)- and Cu(II)-complexes of a hydroxynaphthalene-derived dipicolylamine: fluorescent sensing behaviours toward pyrophosphate ions. Org Biomol Chem 2011;9(22):7774–9.
[33] Oh J, Hong JI. Cation effect on fluorescent sensing of pyrophosphate by a bis(Zn-DPA) probe. Bull Kor Chem Soc 2018;39(7):899–901.
[34] Lee SJ, Rao AS, Shin YH, Chung HJ, Huh Y, Ahn KH, Jung J. A novel method using an acedan-based Zn(DPA) probe to monitor ATP localization in an in vivo system. J Mol Histol 2013;44(2):241–7.
[35] Kumar N, Roopa, Bhalla V, Kumar M. Beyond zinc coordination: bioimaging applications of Zn(II)-complexes. Coord Chem Rev 2021:427.
[36] Yu QQ, Wang MQ. Carbazole-based fluorescent probes for G-quadruplex DNA targeting with superior selectivity and low cytotoxicity. Bioorg Med Chem 2020;28 (17):115641.
[37] Shortreed M, Kopelman R, Kuhn M, Hoyland B. Fluorescent fiber-optic calcium sensor for physiological measurements. Anal Chem 1996;68:1414–8.
[38] Jomová Klaudia, Hudecova Lenka, Lauro Peter, Simunkova Miriama, Alwasel Saleh H, Alhazza Ibrahim M, Valko Marian. A switch between antioxidant and prooxidant properties of the phenolic compounds Myricetin, Morin, 3′,4′-dihydroxyflavone, Taxifolin and 4-hydroxy-coumarin in the presence of copper(II) ions: a spectroscopic, absorption titration and DNA damage study. Molecules 2019; 24(23):4335.
[39] Bhuiya S, Chowdhury S, Haque L, Das S. Spectroscopic, photophysical and theoretical insight into the chelation properties of fisetin with copper (II) in aqueous buffered solutions for calf thymus DNA binding. Int J Biol Macromol 2018; 120:1156–69.
[40] Sohrabi N. Binding and UV/vis spectral investigation of interaction of Ni(II) piroxicam complex with calf thymus deoxyribonucleic acid (Ct-DNA): a Thermodynamic approach. J Pharmaceut Sci Res 2015;7:533–7.
[41] Wang MQ, Zhang Y, Zeng XY, Yang H, Yang C, Fu RY, Li HJ. A benzo(f)quinolinium fused chromophore-based fluorescent probe for selective detection of c-myc G-Quadruplex DNA with a red emission and a large Stocks shift. Dyes Pigments 2019; 168:334–40.
[42] Cheng XH, Liu XJ, Bing T, Cao ZH, Shangguan DH. General peroxidase activity of G-Quadruplex-hemin complexes and its application in ligand screening. Biochemistry 2009;48:7817–23.
[43] Trott O, Olson AJ. Software news and update AutoDock Vina, improving the speed and accuracy of docking with a new scoring function, efficient optimization, and Multithreading. J Comput Chem 2010;31:455–61.